

The 5th International Symposium - Supercritical CO₂ Power Cycles
March 28-31, 2016, San Antonio, Texas

**MATERIALS PERFORMANCE IN SUPERCRITICAL CO₂ IN COMPARISON WITH ATMOSPHERIC
PRESSURE CO₂ AND SUPERCRITICAL STEAM**

Gordon R. Holcomb

Materials Research Engineer
National Energy Technology Laboratory
Albany, OR USA
gordon.holcomb@netl.doe.gov

Ömer N. Doğan

Materials Research Engineer
National Energy Technology Laboratory
Albany, OR USA
omer.dogan@netl.doe.gov

Casey Carney

National Energy Technology Laboratory
and AECOM
Albany, OR USA
casey.carney@netl.doe.gov

Kyle Rozman

National Energy Technology Laboratory
Albany, OR USA
kyle.rozman@contr.netl.doe.gov

Jeffrey A. Hawk

Materials Research Engineer
National Energy Technology Laboratory
Albany, OR USA
jeffrey.hawk@netl.doe.gov

Mark H. Anderson

Research Professor
University of Wisconsin-Madison
Madison, WI USA
manderson@engr.wisc.edu



Gordon Holcomb is a Materials Research Engineer in the Structural Materials Team in the Research & Innovation Center at NETL. He received his Ph.D. from the Ohio State University in Metallurgical Engineering in 1988. Current projects cover corrosion issues in fossil energy systems. He is the U.S. Lead for the Steam Oxidation and Materials for Advanced Boiler and Oxy-combustion Systems tasks in the US-UK Collaboration on Fossil Energy Research and Development, Advanced Materials Technology Area.



Ömer Doğan is a Materials Research Engineer in the Structural Materials Team in the Research & Innovation Center at NETL. He received his Ph.D. from Case Western Reserve University in Materials Science & Engineering in 1990. Current research focuses on the evaluation and development of heat, corrosion, and wear resistant materials for applications in harsh environments.



Casey Carney received his B.S. in chemistry and engineering physics from Hope College. He received his Ph.D. in Chemical Engineering from the University of Colorado in 2005. He is currently an employee of AECOM as a contractor to the United States Department of Energy - National Energy Technology Laboratory in Albany, OR, where he has worked since 2008. His recent research topics have included: oxy-combustion flame analysis, thermal decomposition kinetics, and materials performance in extreme combustion and supercritical CO₂ environments.



Kyle Rozman is a postdoctoral researcher in the Structural Materials Team in the Research & Innovation Center at NETL. Kyle received his Ph.D. from Oregon State University in Materials Science in 2014. He is currently researching the environmental effects on fatigue of iron and nickel superalloys.



Jeffrey Hawk is a Materials Research Engineer in the Structural Materials Team, Materials Engineering and Manufacturing, in the Research & Innovation Center at NETL. He received his Ph.D. from the University of Virginia in Materials Science in 1986. Current projects cover mechanical behavior and microstructural evolution in fossil energy systems.



Mark Anderson is a research professor in the Department of Engineering Physics and Director of the University of Wisconsin's Thermal Hydraulic Laboratory. Dr. Anderson studies the physics, thermal hydraulic performance and material corrosion issues of several different fluids (salts, liquid metals, sH₂O, and sCO₂). He is the U.S. representative to the International Atomic Energy Agency (IAEA) for the coordinated research project on supercritical fluids and has active research on the sCO₂ Brayton cycle for nuclear, solar and fossil advanced power generation.

Abstract

To facilitate the development of supercritical CO₂ (sCO₂) power plants, a comparison of the oxidation behavior of austenitic stainless steel and Ni-base alloys in sH₂O and sCO₂ was made. Experiments were conducted at 730°C/207 bar (sCO₂) and 726°C/208 bar (sH₂O). Ni-base alloys in sCO₂ did not exhibit much change with pressure. Ni-base alloys in sH₂O had an increase in corrosion rate and the log of the parabolic rate constant was proportional to pressure. Austenitic stainless steels in sCO₂ and sH₂O were less protective with pressure as the dense protective chromia scale was replaced with faster growing Fe-oxide rich scales.

Introduction

Heat engine power cycles, using a working fluid of supercritical carbon dioxide (sCO₂) have the potential for high thermodynamic efficiencies when configured as a (indirect) recompression Brayton cycle [1]. Direct cycles, where pressurized oxy-combustion flue gas is utilized as the working fluid in an open loop, are also in development [2]. These sCO₂ cycles are projected to have higher efficiencies compared to steam cycles due to lack of phase change in working fluid within the working envelope, recompression of sCO₂ near liquid densities, and high heat recuperation. In addition to lowering the environmental impact due to the higher efficiencies, dry or reduced water cooling in direct and indirect cycles, and producing storage ready CO₂ in direct cycles, will also lower the environmental impact. Furthermore, compact turbo machinery and simple configurations of the sCO₂ cycles could result in lower capital cost.

While the compactness of the turbo machinery presents the possibility of using more costly alloys (Ni-base superalloys) in fabrication of components to achieve higher efficiency targets, economics dictates to utilize less costly materials to their limits. Materials selection for components exposed to specific sCO₂ power cycles is challenging since materials have not been commonly tested under these conditions. However, materials selected for advanced ultra-supercritical (A-USC) steam (sH₂O) systems are a good starting point for sCO₂ cycles. Required key properties of materials employed in fossil fuel sCO₂ cycles will depend on the application temperature, pressure and environment. In this study, the oxidation behaviour of austenitic stainless steels and Ni-base alloys in sCO₂ and sH₂O will be compared.

Table 1 shows representative proposed inlet and outlet temperatures and pressures for the heater, turbine, and heat exchanger (HX) components of indirect- [3] and direct-cycle [2] sCO₂ power systems. In indirect-cycle systems, the working fluid to expand in the turbine will be relatively pure CO₂. In direct-cycle systems, the working fluid to expand in the turbine will be CO₂-rich combustion gases (for example, CO₂ with 1-5 vol% O₂ and 2-10% vol% H₂O). The work presented here is on environments representative of indirect-cycle systems, with emphasis on the temperatures and pressures associated with the turbine inlet.

Table 1. Representative temperatures and pressures of components in indirect- [3] and direct-cycle [2] sCO₂ power systems. Indirect turbine inlet conditions are the emphasis of the work presented here.

Cycle	Component	Inlet		Outlet	
		T, °C	P, bar	T, °C	P, bar
Indirect	Heater	450-535	10-100	650-750	10-100
	Turbine	650-750	200-300	550-650	80-100
	HX	550-650	80-100	100-200	80-100
Direct	Heater	750	200-300	1150	200-300
	Turbine	1150	200-300	800	30-80
	HX	800	30-80	100	30-80

A few comments on nomenclature are in order for steam power plants. The pressures and temperatures of a pulverized coal (PC) power plant are commonly reported as in this example for the Isogo 1 ultra-supercritical pulverized coal plant: 4060 psi/1050°F/1110°F (280 bar/566°C/599°C) [4]. The pressure and first temperature refer to conditions in superheater tubing and the inlet of the high pressure turbine; the second temperature refers to conditions in the reheater tubing and inlet of the intermediate pressure turbine. The terms subcritical, supercritical (SC), ultra-supercritical (USC), and advanced ultra-supercritical (A-USC) refer to the pressure and temperature of the superheater and inlet of the high pressure turbine. While there are no universally accepted definitions of these terms, they arise out of power plant design and the alloy categories required for operation. Table 2 shows one set of definitions for the steam conditions for each, along with typical net plant efficiency. Due to their high creep strengths at high temperatures, nickel-base superalloys are required for A-USC pulverized coal power plants. Advanced ferritic-martensitic steels and austenitic stainless steels are used in USC power plants. The U.S. convention for net plant efficiency calculations is to use higher heating value (HHV), which includes the heat of steam condensation. The European convention is to use lower heating value (LHV), which does not include the heat of steam condensation—resulting in higher reported efficiencies [5].

Table 2. Steam conditions and net plant efficiencies for various categories of pulverized coal power plants (adapted from ref [5]).

Nomenclature	Typical Conditions	Net Plant Efficiency (HHV)
Subcritical	2400 psi/1050°F/1050°F (165 bar/566°C/566°C)	35%
Supercritical (SC)	3600 psi/1050°F/1075°F 248 bar/566°C/579°C)	38%
Ultra-Supercritical (USC)	>3600 psi/1100°F/1150°F (>248 bar/593°C/621°C)	>42%
Advanced Ultra-Supercritical (A-USC)	4000-5000 psi/1300-1400°F (276-345 bar/704-760°C)	>45%

A comparison of the temperatures and pressures for indirect turbine inlet conditions in sCO₂ (Table 1) and A-USC conditions (Table 2), show how similar the systems are, and why a good starting point for candidate alloys for sCO₂ systems are the ones proposed for A-USC power plants. Bordenet *et al.*

[6] reported long-term testing of Ni-base and austenitic stainless steels under A-USC temperatures from a reheat steam line (21-41 bar), and both the fireside and steamside results showed very low corrosion and oxidation losses. This result, and others (for example in ref [5]), show how these candidate alloys should perform well with respect to steam oxidation in A-USC conditions.

The purpose of this communication is to present and compare results from exposures in sCO₂ and sH₂O. A direct comparison was made for three alloys (austenitic stainless steel 347H and nickel-base superalloys 625 and 282) exposed for (nominally) 500 h at 730°C/207 bar to sCO₂ and sH₂O, and to atmospheric pressure CO₂ (aCO₂) for 500 h at 730°C/1 bar. These results are combined with literature results in both sCO₂ and sH₂O for a comparison of oxidation kinetics in these two systems.

Experimental Procedures

Three alloys were selected for direct comparison in sCO₂, sH₂O and aCO₂. The alloys were 347H austenitic stainless steel and Ni-base alloys 625 and 282. The compositions of each alloy, as determined by wavelength dispersive x-ray fluorescence (WDXRF) using a Rigaku ZSX Primus II spectrometer, are shown in Table 3.

Table 3. Compositions (wt%) of direct comparison alloys as determined by WDXRF (rounded to nearest 0.1). For C, nominal values are given, except for alloy 347H where combustion infrared detection (following ASTM E1019) was used.

Alloy	Fe	Cr	Ni	Co	Mo	Si	Ti	Al	Mn	Cu	V	Nb	C
347H	Bal	17.6	9.1	0.1	0.2	0.3			1.1	0.1	0.1	0.7	0.05
282	0.2	19.4	Bal	10.1	8.7		2.2	1.4					0.06
625	3.4	22.1	Bal		8.9	0.1	0.2	0.1	0.1	0.2		3.3	0.05

Triplicate specimens were made of each alloy for each exposure type. The samples were machined as compact tension specimens with overall dimensions of approximately 23 × 22 × 3 mm. Surfaces were ground to a 600 grit (CAMI, Coated Abrasive Manufacturers Institute, now part of the Unified Abrasives Manufacturers' Association) finish, which is equivalent to a P1200 (FEPA, Federation of European Producers of Abrasives) finish. The samples were then ultrasonically cleaned in isopropyl alcohol, dried, and weighed.

Exposures in sCO₂ were performed in a horizontal autoclave constructed from alloy 625. The autoclave inside diameter was 4.3 cm. The sample rack and exposure specimens are shown in Fig. 1. A SSI Supercritical 24 constant flow dual piston pump was used to inject 99.999% pure CO₂ into the autoclave at a rate of 0.035 kg/hr. At test conditions this resulted in a fluid velocity of 0.4 cm/min through the autoclave, which corresponded to a test section volume change every 2 h. Nominally the test lasted 500 h at 730°C/207 bar. However, there was a loss in pressure from a leak 497.9 h into the test. The autoclave heaters were turned off after 500.5 h of exposure. The temperature averaged 730.4 ± 1.4 °C and the pressure averaged 206.6 ± 0.6 bar.

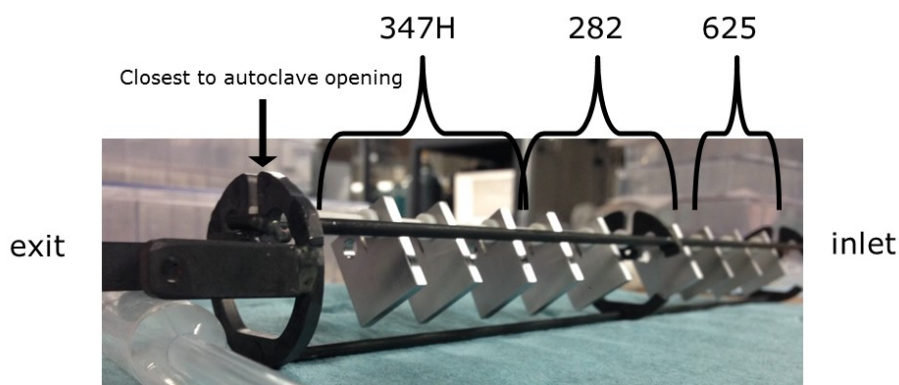


Fig. 1. Sample rack and samples for sCO₂ exposure in a horizontal autoclave. The rack was made from alloy 625 with alumina spacers.

Exposures in sH_2O were performed in a vertical autoclave constructed from alloy 230. The autoclave inside diameter was 6.35 cm. The sample rack and samples are shown in Fig. 2. A Lab Alliance constant pressure dual-piston pump was used to inject deionized water into the autoclave at a rate of 0.27 kg/h. At test conditions this resulted in a fluid velocity of 0.21 cm/min through the autoclave, which corresponded to a test section volume change every 2.4 h. Nominally the test lasted 500 h at 726°C/208 bar. The temperature averaged 725.9 ± 2.4 °C and the pressure averaged 208 ± 3 bar.

Exposures in aCO_2 were performed in a horizontal alumina tube furnace. The tube inside diameter was 6.81 cm. The sample rack and samples are shown in Fig. 3. Carbon dioxide, with a purity of 99.99%, was fed into the tube chamber at a rate of 370 cm³/min, or 0.040 kg/hr. At test conditions this resulted in a fluid velocity of 33 cm/min through the autoclave, which corresponded to a test section volume change every 16 s. Nominally the test lasted 500 h at 730°C/1 bar. A hairline crack was observed in the alumina tube after the test was complete. Subsequently, an oxygen sensor was placed in the tube with the same conditions as the test, except for temperature, which was set at 800°C to enable the stabilized zirconia oxygen sensor to operate. The oxygen partial pressure was measured as 0.25%. Assuming the source of the oxygen was from the atmosphere, a nitrogen partial pressure of 0.93% was inferred.



Fig. 2. Sample rack and samples for sH_2O exposure in a vertical autoclave. Rack hooks were made from alloy 617.

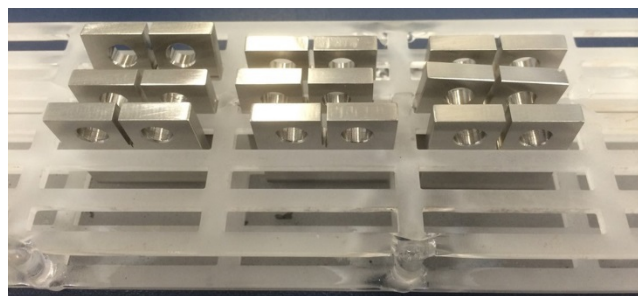


Fig. 3. Sample rack and samples for aCO_2 exposure in a horizontal tube furnace. Rack was of quartz construction.

There was a large difference in linear velocity within the test chambers between the tests at high pressure (0.4 cm/min for sCO_2 and 0.21 cm/min for sH_2O) and the test at atmospheric pressure (33 cm/min for aCO_2). However, when expressed in terms of the Reynolds number, Re , the test

conditions were much more comparable, primarily due to the much higher densities at high pressure. Eq. 1 is the expression for Re,

$$Re = \frac{\rho u L}{\eta} \quad (1)$$

where ρ is the density, u is the velocity, L is a characteristic dimension (chamber diameter in this case), and η is the absolute viscosity. Table 4 summarizes the three direct comparison tests. All of the Re numbers were quite low, indicating laminar flow.

Table 4. Test characteristics summary.

Test	T, °C	P, bar	ρ , g/cm ³	u , cm/min	L, cm	η , Pa*s	Re
sCO ₂	730	207	1.04×10^{-1}	0.40	6.35	4.26×10^{-5}	10.4
sH ₂ O	726	208	4.77×10^{-2}	0.21	4.30	3.89×10^{-4}	1.8
aCO ₂	730	1	5.28×10^{-4}	33.0	6.81	4.14×10^{-5}	4.8

Data collected included mass change measurements, glancing angle (1.5°) x-ray diffraction (XRD), scanning electron microscopy (SEM) of the surfaces of exposed samples using secondary electrons (SE) and back-scattered electrons (BSE), and microanalysis using energy dispersive spectroscopy (EDS). The SEM was a FEI Inspect F50, the EDS was an Oxford INCA, and the XRD was a Rigaku Ultima III.

Results

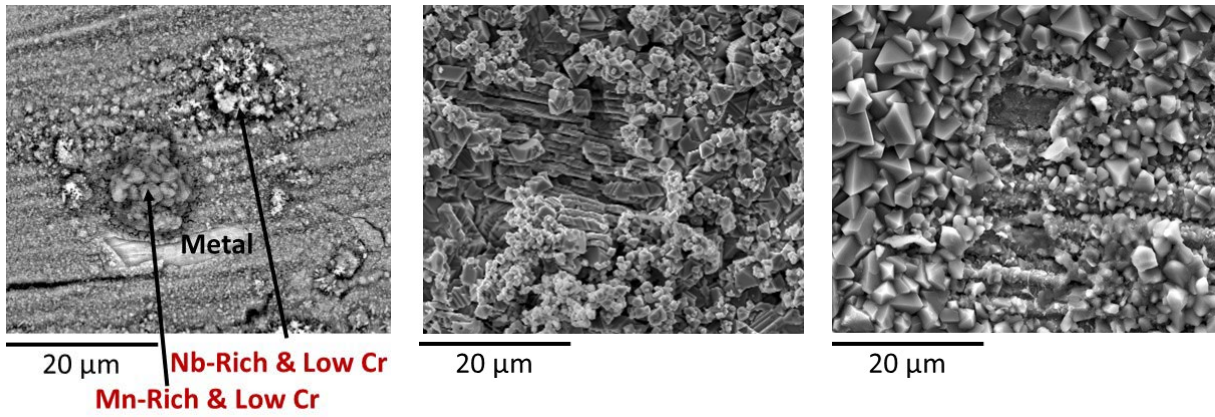
Mass change results are shown in Table 5. In sCO₂, all three alloys had small mass gains—indicative of the formation of a thin protective chromia scale. In sH₂O, the mass gains for alloy 347H were very high for two of the replicates, and small for the third replicate. Examination of the surface of the third replicate with a small mass gain showed evidence of spalling (i.e., areas where some of the oxide remained and areas without the thick oxide layer). The two Ni-base alloys had higher mass gains in sH₂O than in sCO₂, and with more variability, but these mass increases were relatively small. In aCO₂, the negative mass change values for alloy 347H was clear evidence of oxide spalling. The mass change values for the two Ni-base alloys for aCO₂ were similar to those found for sCO₂.

Table 5. Mass change (mg/cm²) results after 500 h.

Alloy	sCO ₂	sH ₂ O	aCO ₂
347H	0.10	8.44	-2.47
	0.08	7.58	-3.33
	0.08	0.79	-3.23
282	0.36	0.87	0.40
	0.33	1.25	0.42
	0.33	0.39	0.37
625	0.16	2.73	0.09
	0.15	0.53	0.08
	0.21	0.31	0.07

Surface SE SEM results are shown in Fig. 4 for alloy 347H. In sCO₂ (Fig. 4a), most of the surface was a thin Cr-rich oxide. However, there were also areas of thicker oxides that were either Mn-rich or Nb-rich, as well as some areas without oxide indicative of a spall. Glancing angle XRD showed the surface to contain Cr₂O₃ and M₃O₄ phases.¹ The exposures in sH₂O and aCO₂ (Figs. 4b-4c) consisted of Fe₂O₃ with small amounts of Cr, Mn, and Ni (based on combined XRD and EDS analysis).

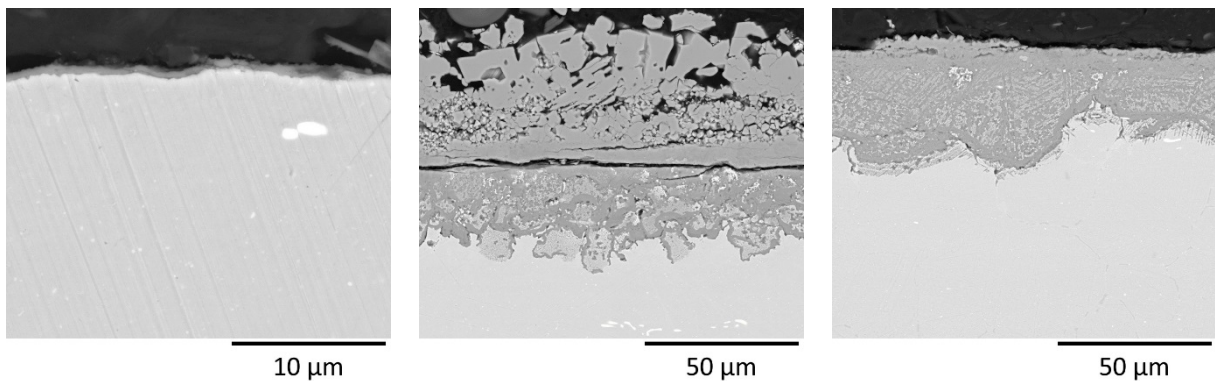
¹ The XRD signal from MnFe₂O₄, Mn₃O₄, Fe₂NiO₄, Mn₂NiO₄ and Fe₃O₄ are all quite similar, so reporting as M₃O₄ is generally more accurate.



(a) $s\text{CO}_2$, $+0.08 \text{ mg/cm}^2$ (b) $s\text{H}_2\text{O}$, $+7.62 \text{ mg/cm}^2$ (c) $a\text{CO}_2$, -3.33 mg/cm^2

Fig. 4. Surface SE SEM results for alloy 347H after 500 h of exposure. The mass change values identify the specific sample imaged from Table 5.

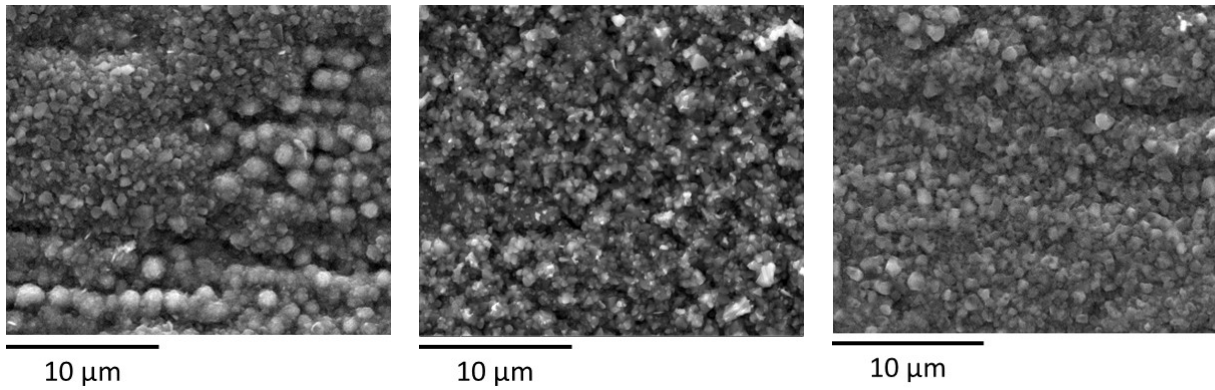
Cross-section BSE SEM results are shown in Fig. 5 for alloy 347H. A thin and protective chromia scale formed in $s\text{CO}_2$, as seen in Fig. 5a. Thick oxide scales formed in both $s\text{H}_2\text{O}$ and $a\text{CO}_2$, Fig. 5b and Fig. 5c, respectively. Elemental mapping for $s\text{H}_2\text{O}$ shows an outer iron oxide scale ($\sim 40\mu\text{m}$). Below that was a mixed oxide region ($\sim 30\mu\text{m}$) that was overall rich in Cr and Mn, poor in Fe, with both rich and poor areas of Ni, as well as a few Nb regions. Patches of an internal oxidation region of 39O-37Fe-13Cr-11Ni were observed. The mass loss measurements in $a\text{CO}_2$ indicated that the outer portion of the scale spalled. While Fig. 5c was representative of most of the surface, there were small areas with retained outer oxide, which was pure iron oxide about 20-25 μm thick. The remaining scale in $a\text{CO}_2$ had several composition (at%) bands: 1) nearest the outer surface, to a depth of about 8 μm , was 67O-17Fe-11Cr-4Ni, 2) below that, with a thickness of about 15 μm , was 62O-16Fe-14Cr-6Ni, 3) below that was a thin ($\sim 3 \mu\text{m}$) layer of 64O-17Fe-18Cr, and 4) an internal oxide layer ($\sim 8 \mu\text{m}$ thick) with 42O-32Fe-13Cr-11Ni. Internal oxidation is likely in the form of chromia.



(a) $s\text{CO}_2$, $+0.10 \text{ mg/cm}^2$ (b) $s\text{H}_2\text{O}$, $+8.44 \text{ mg/cm}^2$ (c) $a\text{CO}_2$, -2.47 mg/cm^2

Fig. 5. Cross-section BSE SEM results for alloy 347H after 500 h of exposure. The mass change values identify the specific sample imaged from Table 5.

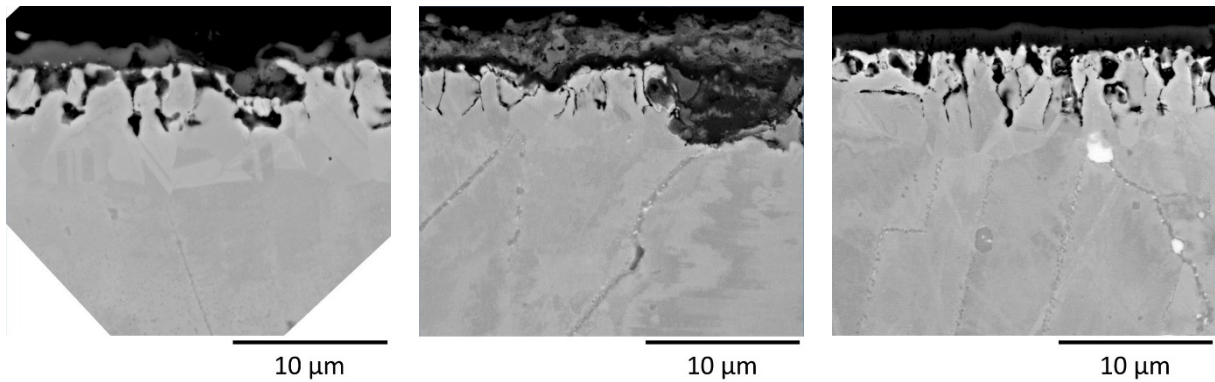
Surface SE SEM results are shown in Fig. 6 for alloy 282. The surfaces of all three exposures were similar in appearance, with small sub-micron oxide particles. Glancing angle XRD showed the primary surface phases to be Cr_2O_3 and TiO_2 , which is in agreement with EDS analysis.



(a) $s\text{CO}_2$, $+0.33 \text{ mg/cm}^2$ (b) $s\text{H}_2\text{O}$, $+1.25 \text{ mg/cm}^2$ (c) $a\text{CO}_2$, $+0.42 \text{ mg/cm}^2$

Fig. 6. Surface SE SEM results for alloy 282 after 500 h of exposure. The mass change values identify the specific sample imaged from Table 5.

Cross-section BSE SEM results are shown in Fig. 7 for alloy 282. The structures in $s\text{CO}_2$ and $a\text{CO}_2$ were similar to each other. The oxide scale was thicker in $s\text{H}_2\text{O}$ than in CO_2 , while internal oxidation was deeper in CO_2 . In CO_2 , the oxide scale was primarily Cr oxide (glancing angle XRD indicated Cr_2O_3), with Ti oxide (TiO_2) as a secondary component. In $s\text{H}_2\text{O}$, the oxide scale had thin Cr-rich layers. Where Cr was not enriched, it also had Ni, Co, and Ti oxides. Internal oxidation consisted of Al and Ti oxides, with Ti oxide found near the alloy/oxide interface and Al oxide found at all internal oxide locations. The alloy matrix was depleted in Cr, Al and Ti to a depth about 50-100% deeper than the internal oxidation depth. This is shown in Fig. 8 for exposure in $s\text{CO}_2$. Alloy 282 is strengthened by gamma prime, $\text{Ni}_3(\text{Al,Ti})$, so loss of Al and Ti will lower alloy strength to this depth, and not just by metal thickness loss.



(a) $s\text{CO}_2$, $+0.36 \text{ mg/cm}^2$ (b) $s\text{H}_2\text{O}$, $+0.87 \text{ mg/cm}^2$ (c) $a\text{CO}_2$, $+0.40 \text{ mg/cm}^2$

Fig. 7. Cross-section BSE SEM results for alloy 282 after 500 h of exposure. The mass change values identify the specific sample imaged from Table 5.

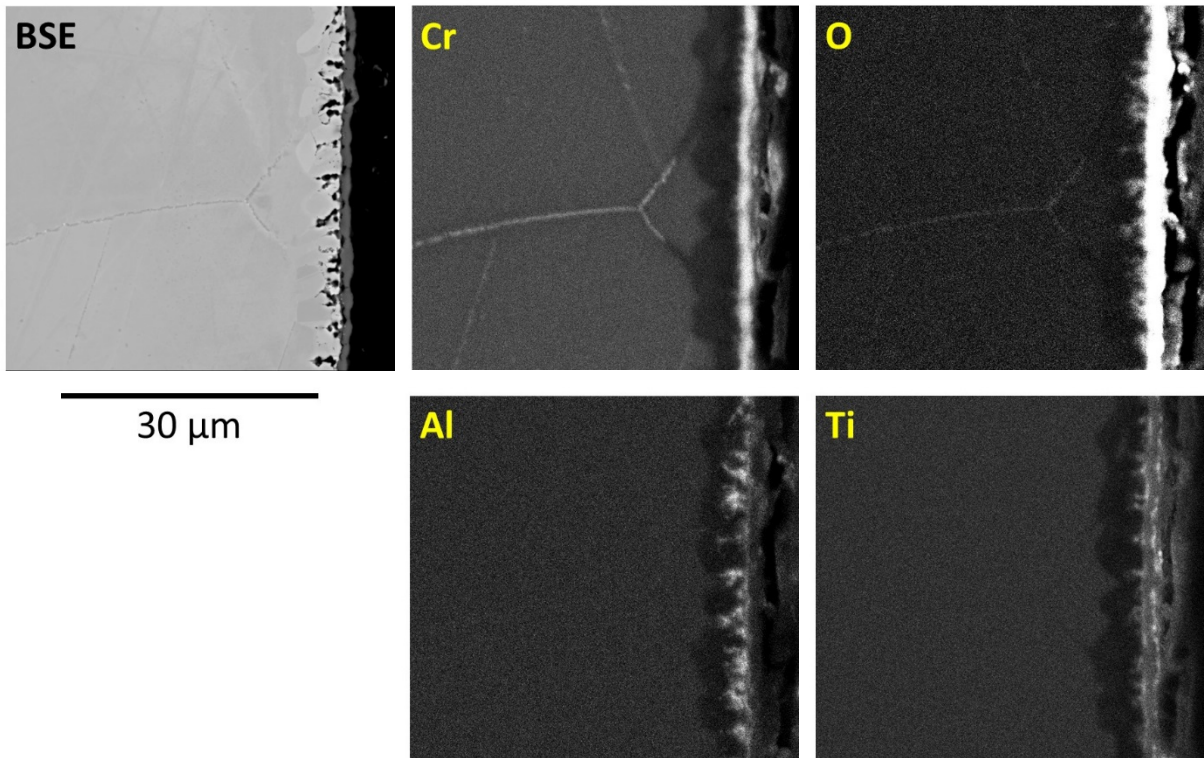


Fig. 8. Elemental mapping of alloy 282 by EDS after 500 h of exposure in sCO₂ at 730°C and 207 bar.

Surface SE SEM results are shown in Fig. 9 for alloy 625. The surfaces look similar to that for alloy 282 in Fig. 6, except that some of the oxide particles in aCO₂ (Fig. 9c) were larger in size. Glancing angle XRD showed the primary surface phase to be Cr₂O₃, which is in agreement with EDS analysis.

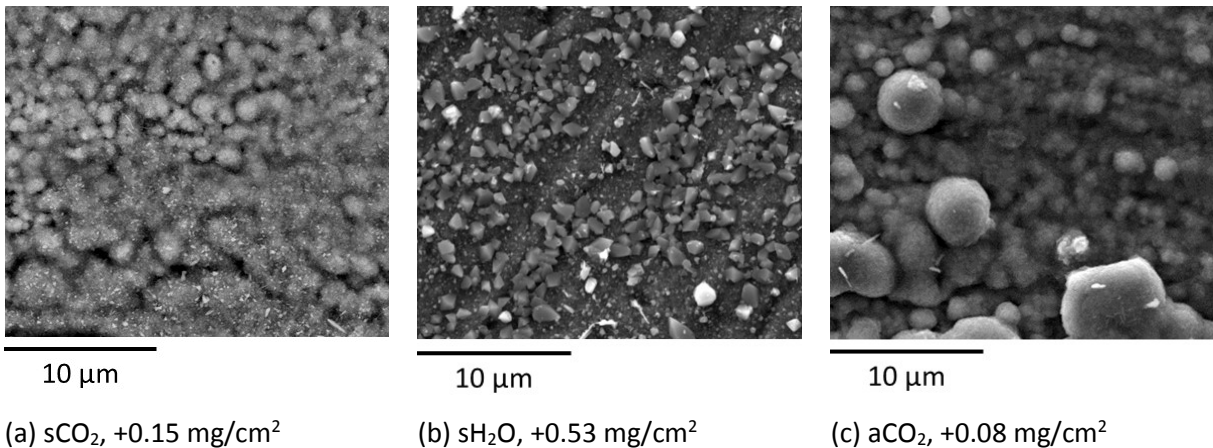


Fig. 9. Surface SE SEM results for alloy 625 after 500 h of exposure. The mass change values identify the specific sample imaged from Table 5.

Cross-section BSE SEM results are shown in Fig. 10 for alloy 625. The oxide scale in both sCO₂ (Fig. 10a) and aCO₂ (Fig. 10c) were Cr oxides (Cr₂O₃) with some Ni and a trace amount of Mn. Bright second phases were Nb/Mo rich. There was enrichment of Nb and Mo in the alloy near the oxide scale. Some portions of the aCO₂ cross-section had thicker scales than in Fig. 10(c), especially along the original edges. In sH₂O, Table 5 shows two results with very low oxidation rates and one with a high oxidation rate. Figure 10b is the cross-section of the high oxidation rate sample, showing a very thick oxide scale (note the scale marker change). The composition of the scale had metal ratios similar to that of the alloy, indicating that a protective scale was not formed. The other two samples of alloy 625 in sH₂O had very low oxidation rates and Cr₂O₃ was detected at the surface by glancing

angle XRD. This indicates that these two samples established and maintained a chromia scale. It is not known what triggered the change in behaviour among the sH₂O samples.

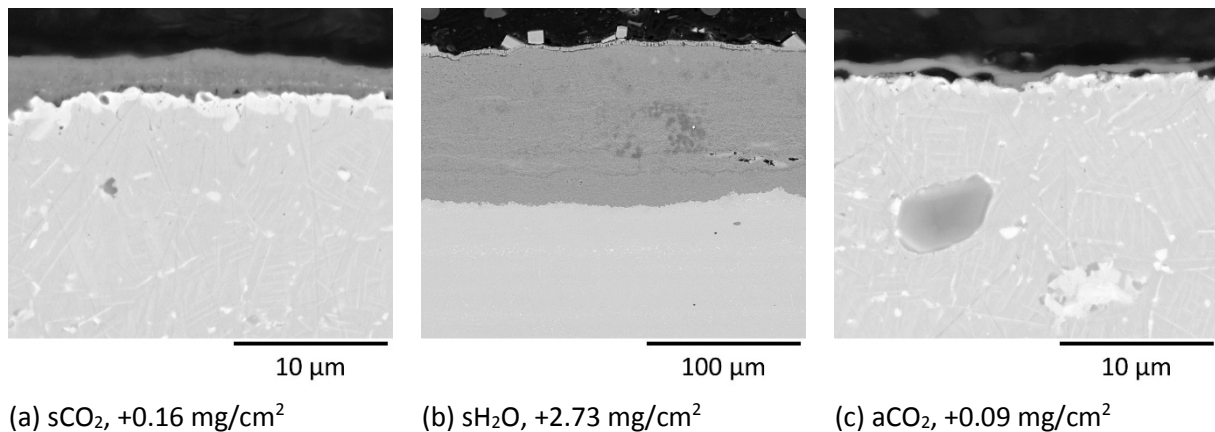


Fig. 10. Cross-section BSE SEM results for alloy 625 after 500 h of exposure. The mass change values identify the specific sample imaged from Table 5.

Discussion

Mass gain results were put into parabolic form for ease of comparison with literature values for these and similar alloys. The validity and some of the limitations of this approach has been discussed in Holcomb *et al.* [7]. Equation 2 shows how the parabolic rate constant, k_p , was defined, where Δm is mass change and t is time. This calculation was not done when there was evidence of spalling.

$$k_p = \frac{(\Delta m)^2}{2t} \quad (2)$$

sH₂O Environments

A comparison of the parabolic rates for the experimental results in sH₂O with those in the literature for 300 series stainless steels (nominally Fe-18Cr-8Ni) is made in Fig. 11. Averages of triplicate experimental test results are shown. Some of the earlier experimental test results are shown [7,9], including those for E-Brite, a high Cr ferritic stainless steel. At atmospheric pressure, parabolic rates for fine-grained alloys align with that of a pure chromia scale—the PMCr data [8]. Coarse-grained alloys oxidize much faster and do not maintain a dense and compact chromia scale. At higher pressures, Fig. 11 shows most results for fine-grain alloys having higher corrosion rates than at atmospheric pressure; in some cases similar to what would be expected for coarse-grain alloys. The experimental test alloys had ASTM grain sizes of 7 for 304H, 10 for alloy 347H, and 9 for E-Brite. While there is no definitive definition, a grain size of 5 or greater is the general dividing point for these alloys to be considered fine-grained. The high pressure test data for fine-grained 304H show the full range of results, from values close to the PMCr line to those of the coarse-grained atmospheric pressure line. E-Brite, with a higher Cr value and a very fine grain size, was close to the PMCr line in both cases. Examination of the surfaces of samples with SEM showed that very low oxidation rate surfaces were primarily chromia, and very high oxidation rate surfaces were primarily iron oxides (containing a small amount of chromium). Surfaces with oxidation rates between the two extremes had nodules, or islands, of iron oxide against a chromia background. The breakdown in the protective chromia scale resulted in the nucleation of sites with faster growing iron oxides that grow laterally to eventually cover the surface. Nucleation events can vary with time, leading to the range in oxidation behavior observed in Fig. 11. In summary, elevated pressure exposures of fine-grained 300 series stainless steels increased the oxidation rate, making them behave more like coarse-grained alloys.

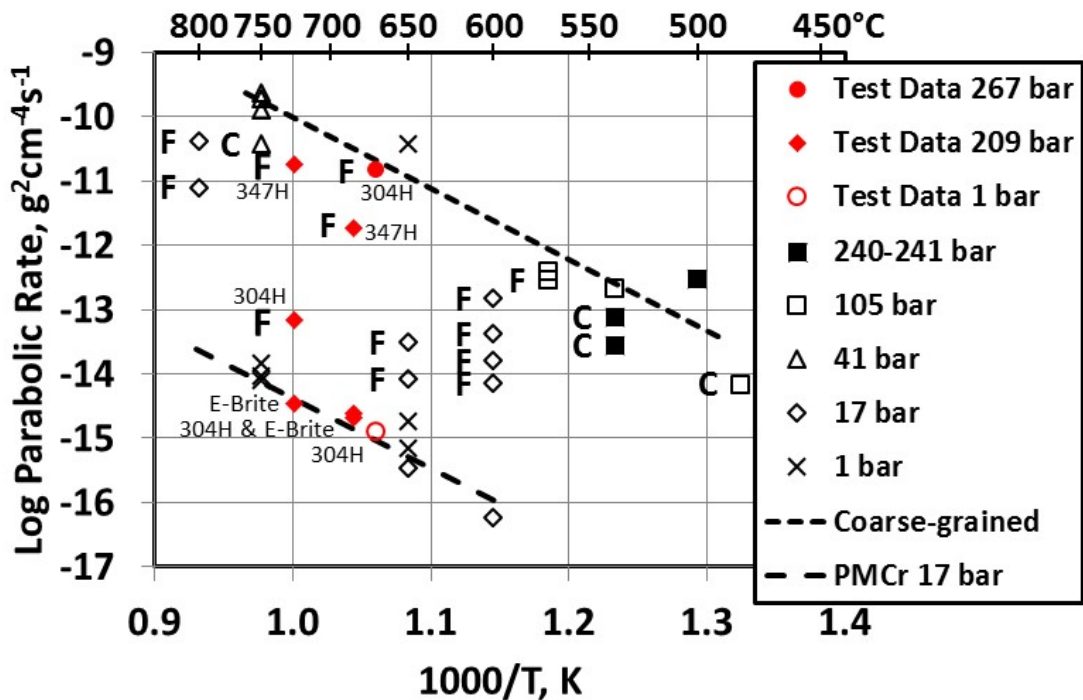


Fig. 11. Arrhenius plot of parabolic oxidation of 300 series austenitic stainless steels (nominally Fe-18Cr-8Ni alloys) in steam, updated from Holcomb [9] and Holcomb *et al.* [7], which was adapted from the compilation of Wright and Dooley [10] with numerous sources for coarse-grain alloys: 241 bar (304 and 347 at 538°C) [11], 240 bar (316 at 500°C) [12], 105 bar (304 at 482 and 538°C) [13], 41 bar (304, 316, 321, and 347) [14], and 1 bar (304 at 650°C, $-10.4 \log(\text{g}^2\text{cm}^{-4}\text{s}^{-1})$) [15]; and fine-grain alloys: 105 bar (304HFG and 347HFG at 571°C) [16], 17 bar (347HFG, CF8C and S304H) [8], and 1 bar (all other 1 bar data, 304H, 347HFG, S304H) [17]. The 17 bar PMCr data [8] is for a pure chromia forming alloy. CF8C is a cast version of 347. The C and F labels indicate coarse- and fine-grain alloys when away from the coarse-grain fit and PMCr lines. Test data at both 208 and 209 bar are labeled as 209 bar.

A comparison of the parabolic rates for the experimental results in sH_2O with those in the literature for Ni-base alloys is made in Fig. 12. Averages of triplicate experimental test results are shown, along with some from earlier tests [7, 9]. At atmospheric pressure, parabolic rates align with that of a pure chromia scale—the PMCr data [8]. The high pressure test data, 190 bar and above, showed significantly higher oxidation rates. One result, for alloy 625 at 670°C and 267 bar, showed a much higher oxidation rate. As described in Holcomb [9], the scale was very thick and had metal composition ratios (not including oxygen) similar to that of the alloy. This is similar to what was observed in Fig. 10b. Grain size, composition, and expected phases were examined as possible sources of the difference between alloy 625 and the other alloys, but no conclusions were established. Long-term exposure of alloy 625 in a power plant test of over 8000 h [18] showed very good oxidation behavior (the lower of the two 190 bar data points in Fig. 12). That, combined with a failure to reproduce such high oxidation rates in subsequent tests, has led to considering the very high oxidation result for alloy 625 at 267 bar to be an outlier. Another apparent outlier is the 41 bar result for alloy 600 [14]. This alloy has 15.5% Cr, which is less than the other alloys shown in Fig. 12. This could have contributed to the development of a less protective oxide scale. The oxides grown on Ni-base alloys at high pressures were thicker than at low pressures, but were still primarily chromia scales. In summary, elevated pressure exposures of Ni-base alloys increased the oxidation rate by 1-2 orders of magnitude. It should be noted that these are still relatively low oxidation rates, and would not preclude the successful use of Ni-base alloys in A-USC power plant applications.

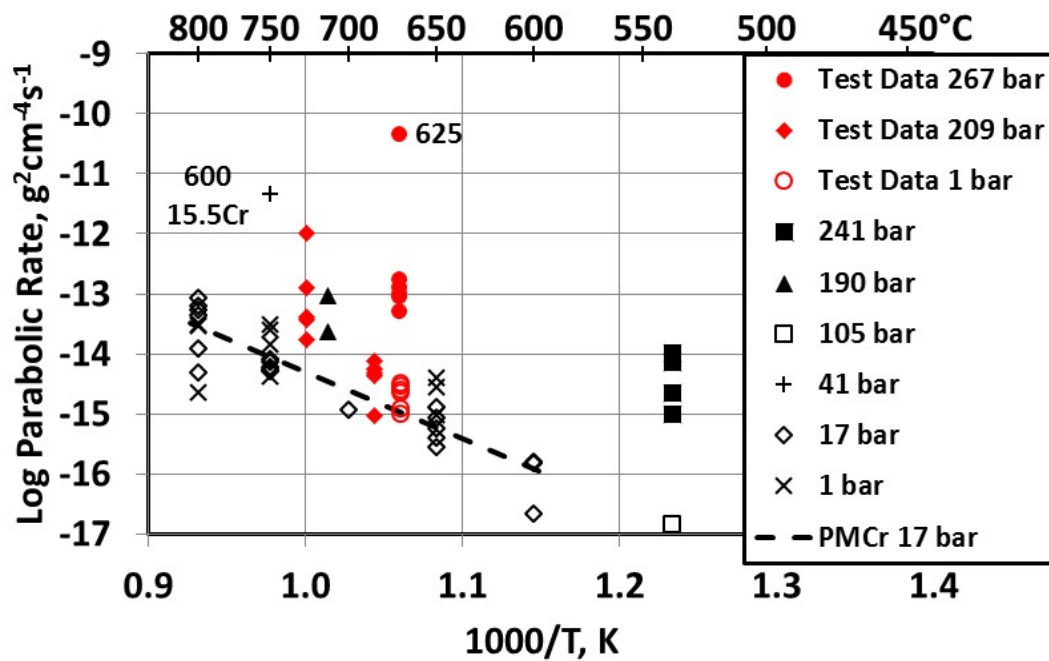


Fig. 12. Arrhenius plot of parabolic oxidation of Ni-base alloys in steam, updated from Holcomb [9 and Holcomb *et al.* [7], which was adapted from the compilation of Wright and Dooley [8] from numerous sources: 241 bar (600, 601, 718) [11], 105 bar (617) [13], 41 bar (600) [14], 17 bar (230, 617, 718, 740, 263, 80A, PMCr) [8], and 1 bar (230, 617, 740, and 263 [17]. In addition, long-term industrial exposures of 625 and Waspalloy at 1 bar (750°C) and 190 bar (713°C) were added [18]. The 17 bar PMCr data [8] is for a pure chromia forming alloy. Test data at both 208 and 209 bar are labeled as 209 bar.

sCO₂ Environments

To supplement the *sCO₂* experimental results for a comparison with *sH₂O*, mass loss data from the literature was examined. The examination was limited to results using research grade *CO₂* (at least 99.99% pure) and at 200-220 bar. Many results were performed for a single time interval. These were treated in the same manner as the experimental results, with k_p values estimated using Eq. 2.

Other results had a series of times and mass changes. In cases where initial oxidation does not follow parabolic kinetics, it is preferable to calculate the parabolic rate constant from the slope of Δm vs the square root of time (t), rather than directly from Δm^2 vs t [19]. The Δm vs the square root of t procedure was used here. Initial oxidation may include either the formation of non-protective scales prior to the establishment of a more protective scale, or the transition from a short-lived more protective oxide to a less protective oxide. In some cases the data fit parabolic kinetics better after an initial period of time rather than starting at time equal to zero. Excluding some of the initial mass change data can improve the determination of k_p . To consistently quantify the decision to obtain k_p after an initial period of time, the F-statistic (using the Linest function in Excel) was used [20]. The literature data sets with 4 or more data points were examined with the F-statistic using all the data prior to any maximum in mass change (which would indicate spalling and non-parabolic behavior). Subsequently, all but the first data point was analyzed, then all but the first two data points, and so on. The data set with at least four data points and with the maximum F-statistic was used to obtain k_p , with the proviso that a majority of the data were used.

A comparison of the parabolic rates for the experimental results in *sCO₂* with those in the literature for 300 series stainless steels (nominally Fe-18Cr-8Ni alloys) is made in Fig. 13. For ease in making comparisons with the *sH₂O* data in Fig. 11, the PMCr 17 bar data in steam [8] indicating protective chromia formation and coarse-grained behavior in atmospheric pressure steam [10] indicating less-

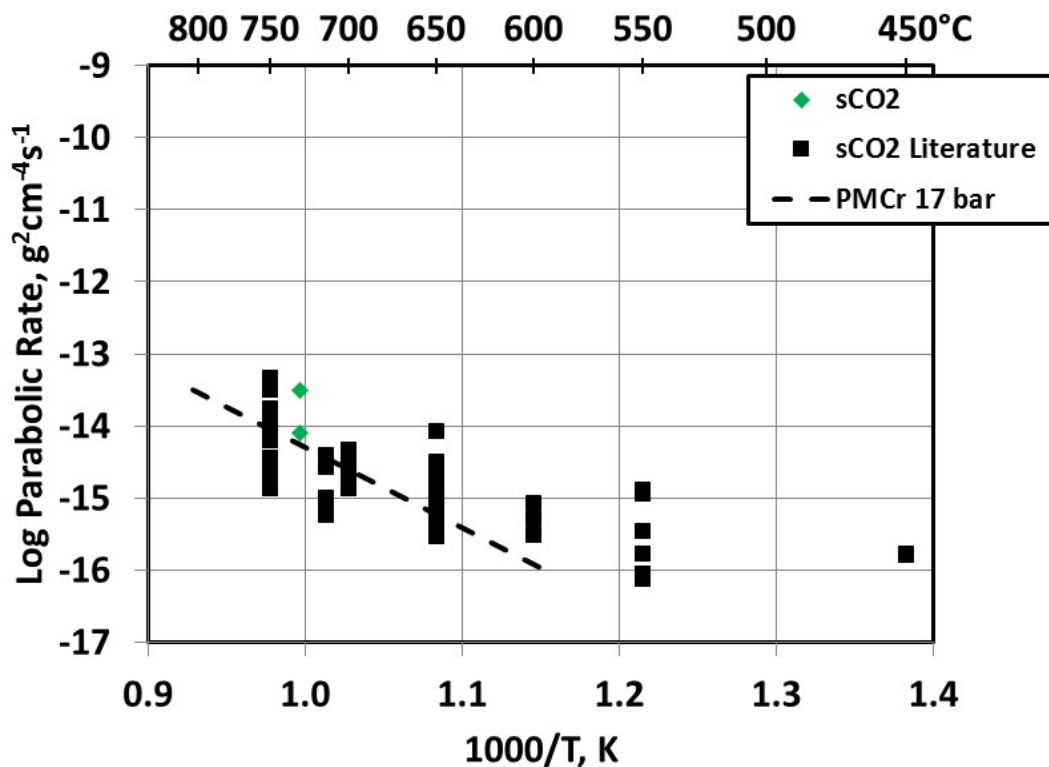


Fig. 14. Arrhenius plot of parabolic oxidation of Ni-base alloys in $s\text{CO}_2$ at 200-207 bar. Literature values were derived from [23, 26-31]. For comparison purposes, the 17 bar PMCr data in steam [8] for a pure chromia forming alloy was included.

$a\text{CO}_2$ Environments

The very low mass change results for the two Ni-base alloys in $a\text{CO}_2$ and $s\text{CO}_2$ (Table 5) were very similar and showed little variability with pressure. Figure 14 shows that the kinetics in $s\text{CO}_2$ were consistent with protective chromia scale formation. The kinetics in $a\text{CO}_2$ were as well. The similar kinetics, combined with the similar surface scale morphologies (Figs. 6 and 9), show that pressure had very little influence on the oxidation behavior of Ni-base alloys—at least within the first 3000 h (the longest duration of the tests reported in Fig. 14 [27]).

The results in $a\text{CO}_2$ for the austenitic alloy 347H was markedly different than in $s\text{CO}_2$. In $s\text{CO}_2$, a thin protective chromia scale covered much of the surface, Fig. 4a. In $a\text{CO}_2$, the mass change results (Table 5) indicated spalling occurred. The observable scale was primarily iron oxide, Fig. 4c. This result is consistent with the variable effect of pressure shown in Fig. 13. At times iron-rich nodules can form, which spread to cover the surface. These iron-rich oxides are less protective than the chromia scales, and grow much thicker. Thick oxides are more prone to spallation than thin oxides, so the mass loss found in $a\text{CO}_2$ was not a surprising result.

Effect of Pressure on Oxidation Kinetics

To isolate and estimate the pressure effect in steam from the experimental and literature results at different pressures and temperatures, the activation energy for chromia formation using the PMCr 17 bar data [8] was determined (207 kJ/mol). Since oxide scales remained essentially pure chromia at high pressure, Arrhenius behavior was assumed and the activation energy used to estimate what the data in Fig. 12 would be at 700°C.

For Ni-base alloys the estimates on a 700°C basis are shown in Fig. 15. The two outliers in the data set (data points denoted by \times in Fig. 15) were not used to fit the data. In Fig. 15a, the log k_p values are

shown in terms of $\log P_T$. There was a large amount of scatter in the data, and the R^2 value was 0.33. In Fig. 15b, the $\log k_p$ values are shown in terms of P_T . The fit was better, with an R^2 value of 0.60. The fit was better largely due to less pressure dependence in the data at 17 bar. Based on this analysis, the effect of pressure on $\log k_p$ appears to be proportional to P_T .

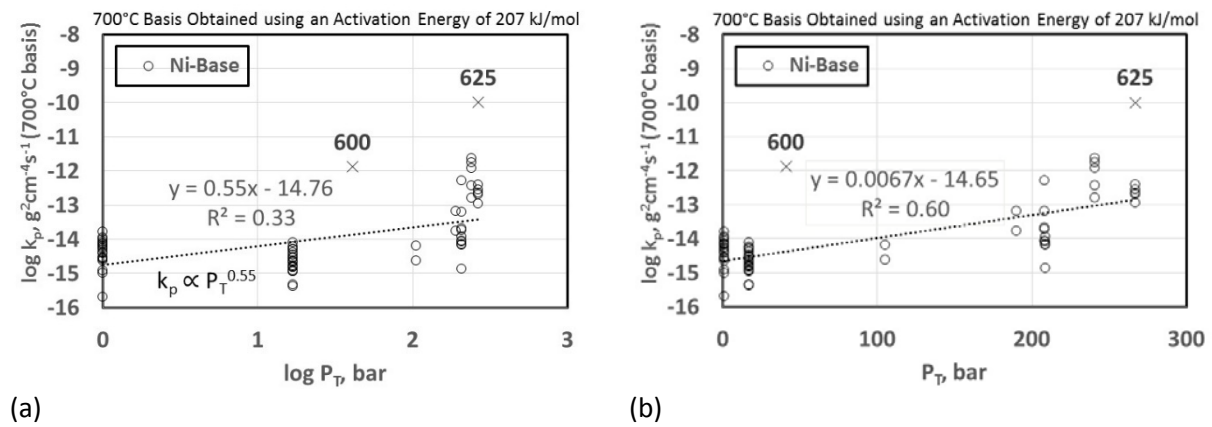


Fig. 15. Oxidation kinetics of Ni-base alloys as a function of pressure using an activation energy of 207 kJ/mol to estimate the data on a 700°C basis.

Conclusions

A comparison of the oxidation behavior of austenitic stainless steels and Ni-base alloys in sH_2O and sCO_2 was made. Experiments were conducted at 730°C and 207 bar (sCO_2) and 726°C and 208 bar (sH_2O).

Ni-base alloys in sCO_2 did not exhibit much, if any, effect on oxidation behavior with pressure. Dense and protective chromia scales were formed. In contrast, Ni-base alloys in sH_2O had an increase in corrosion rates and parabolic rate constants as a function of pressure. Chromia scales still formed, but were less protective. It should be noted that these are still relatively low oxidation rates, and would not preclude the successful use of Ni-base alloys in A-USC power plant applications. A relationship of $\log k_p$ being proportional to P_T in sH_2O was found from an examination of the experimental and literature data.

Austenitic stainless steels in sCO_2 and sH_2O responded similarly with pressure. In both cases the dense protective chromia scale that formed at atmospheric pressure was replaced by faster growing Fe-oxide rich scales. Variability in the nucleation of Fe-oxide nodules on the surface led to a lot of variability in the oxidation kinetics.

The oxidation behavior of candidate A-USC alloys was found to be as good as, or better, in sCO_2 than in sH_2O . So it was confirmed, based on relatively short-term oxidation tests, that these alloys are also good candidates for indirect sCO_2 power system components.

Acknowledgements

This work was funded by the Advanced Combustion Program at the National Energy Technology Laboratory (Richard Dennis and Daniel Driscoll, Technology Managers and Briggs White, Project Monitor). The Research was executed through NETL's Research and Innovation Center's Advanced Combustion Field Work Proposal.

The authors would also like to thank Arjun Kalra and Paul Brooks at the University of Wisconsin—Madison for their work on sCO_2 exposures.

Disclaimer

This report was prepared as an account of work sponsored by an agency of the United States Government. Neither the United States Government nor any agency thereof, nor any of their employees, makes any warranty, express or implied, or assumes any legal liability or responsibility for the accuracy, completeness, or usefulness of any information, apparatus, product, or process disclosed, or represents that its use would not infringe privately owned rights. Reference herein to any specific commercial product, process, or service by trade name, trademark, manufacturer, or otherwise does not necessarily constitute or imply its endorsement, recommendation, or favoring by the United States Government or any agency thereof. The views and opinions of authors expressed herein do not necessarily state or reflect those of the United States Government or any agency thereof.

References

- [1] R.A. Dennis, "U.S. DOE R&D Program on Supercritical CO₂ Power Cycles," in Proceedings: EPRI International Conference on Corrosion in Power Plants, EPRI-3002006972, Palo Alto, CA, 2015, 3002006972, pp. 2-136 to 2-153.
- [2] R.J. Allam, "NET Power's CO₂ cycle: the breakthrough that CCS needs," in Modern Power Systems, <http://www.modernpowersystems.com/features/featurenet-powers-co2-cycle-the-breakthrough-that-ccs-needs/>, 2013.
- [3] G.A. Johnson, M.W. McDowell, G.M. O'Connor, C.G. Sonwane, and G. Subbaraman, "Supercritical CO₂ Cycle Development at Pratt & Whitney Rocketdyne," in Proceedings of ASME Turbo Expo 2012 GT2012, paper 70105, ASME, Copenhagen, Denmark, 2012, pp. 1-10.
- [4] R. Viswanathan, A.F. Armor, and G. Booras, *Power*, 148, 3(2004) 42-49.
- [5] "U.S. Department of Energy and Ohio Coal Development Office Advanced Ultra-Supercritical Materials Project for Boilers and Steam Turbines - Summary of Results," EPRI 1022770, Palo Alto, CA, 2011, pp. 24.
- [6] B. Bordenet, R. Ganta, L. Antony, S. Goodstine, J. Marion, and . Pschirer, "Steam Oxidation and Fireside Corrosion Testing of Several Advanced Alloys in a Steam Loop at A-USC Design Temperatures," in Proceedings: EPRI International Conference on Corrosion in Power Plants, EPRI-3002006972, Palo Alto, CA, 2015, pp. 7-2 to 7-21.
- [7] G. R. Holcomb, C. Carney, and Ö. Doğan, "Oxidation of Alloys for Energy Applications in Supercritical CO₂ and H₂O," submitted to *Corrosion Science*, January 13, 2016.
- [8] I.G. Wright, P.F. Tortorelli, and M. Schütze, "Program on Technology Innovation: Oxide Growth and Exfoliation on Alloys Exposed to Steam," EPRI 1013666, Palo Alto, CA, 2007.
- [9] G. Holcomb, *Oxid Met*, 82 (2014) 271-295.
- [10] I.G. Wright and R.B. Dooley, *International Materials Reviews*, 55 (2010) 129-167.
- [11] H.E. McCoy and B. McNabb, "Corrosion of Several Metals in Supercritical Steam at 538°C," Oak Ridge National Laboratory ORNL/TM-5781, Oak Ridge, TN, 1977, pp. 51.
- [12] M. Sun, X. Wu, Z. Zhang, and E.-H. Han, *Corrosion Science*, 51 (2009) 1069-1072.
- [13] J.C. Griess and W.A. Maxwell, "The Long-Term Oxidation of Selected Alloys in Superheated Steam at 482 and 538° C," Oak Ridge National Laboratory ORNL-5771, Oak Ridge, TN, 1981, pp. 46.
- [14] W.E. Ruther, R.R. Schlueter, R.H. Lee, and R.K. Hart, *Corrosion*, 22 (1966) 147-155.
- [15] V. Lépingle, G. Louis, D. Petelot, B. Lefebvre, and J.C. Vaillant, *Materials Science Forum*, 369-372 (2001) 239-246.
- [16] H. Matsuo, Y. Nishiyama, and T. Yamadera, "Steam Oxidation of Fine-Grain Steels," in R. Viswanathan, D. Gandy, and K. Coleman (Eds.) *Advances in Materials Technology for Fossil Power Plants*, ASM International, Materials Park, OH, 1995, pp. 441-451.
- [17] J. Sarver, private communication from J. Sarver, Babcock & Wilcox, to I.G. Wright, Oak Ridge National Laboratory, 2009.
- [18] R. Knödler and S. Straub, *Oxid Met*, 82 (2014) 113-122.

- [19] B. Pieraggi, *Oxid Met*, 27 (1987) 177-185.
- [20] G.R. Holcomb, P.D. Jablonski, and P. Wang, "Cast Alloys for Advanced Ultra Supercritical Steam Turbines," in E.A. Ott, J.R. Groh, A. Banik, I. Dempster, T.P. Gabb, R. Helmink, X. Liu, A. Mitchell, G.P. Sjöberg, and A. Wusatowska-Sarnek (Eds.) 7th International Symposium on Superalloy 718 and Derivatives, John Wiley & Sons, Inc, Pittsburgh, PA, 2010, pp. 947-960.
- [21] T. Furukawa, Y. Inagaki, and M. Aritomi, *Progress in Nuclear Energy*, 53 (2011) 1050-1055.
- [22] G. Cao, V. Firouzdor, K. Sridharan, M. Anderson, and T.R. Allen, *Corrosion Science*, 60 (2012) 246-255.
- [23] B.A. Pint and J.A. Keiser, "The Effect of Temperature on the sCO₂ Compatibility of Conventional Structural Alloys," in 4th International Symposium - Supercritical CO₂ Power Cycles, Pittsburgh, PA, 2014, pp. 1-13.
- [24] J.Y. Lim, T.J. McKrell, G. Eastwick, and R.G. Ballinger, "Corrosion of Materials in Supercritical Carbon Dioxide Environments," in *Corrosion 2008*, paper 08430, NACE International, New Orleans, LA, 2008.
- [25] R.I. Olivares, D.J. Young, P. Marvig, and W. Stein, *Oxid Met*, 84 (2015) 585-606.
- [26] M.W. Dunlevy, "An Exploration of the Effect of Temperature on Different Alloys in a Supercritical Carbon Dioxide Environment," M.S. Thesis, Department of Nuclear Science and Engineering, Massachusetts Institute of Technology, 2007, pp. 176.
- [27] H.J. Lee, H. Kim, S.H. Kim, and C. Jang, "Comparison of the Corrosion Behaviors of Fe-base and Ni-base Austenitic Alloys in High Temperature S-CO₂ Environment," in *Proceedings: EPRI International Conference on Corrosion in Power Plants*, EPRI-3002006972, Palo Alto, CA, 2015, pp. 3-47 to 3-63.
- [28] H.J. Lee, H. Kim, and C. Jang, "Compatibility of Candidate Structural Materials in High-temperature S-SO₂ Environment," in 4th International Symposium - Supercritical CO₂ Power Cycles, Pittsburgh, PA, 2014, pp. 1-9.
- [29] V. Firouzdor, K. Sridharan, G. Cao, M. Anderson, and T.R. Allen, *Corrosion Science*, 69 (2013) 281-291.
- [30] V. Dheeradhada, A. Thatte, M. Karadge, and M. Drobnjak, "Corrosion of Supercritical CO₂ Turbomachinery Components," in *Proceedings: EPRI International Conference on Corrosion in Power Plants*, EPRI-3002006972, Palo Alto, CA, 2015, pp. 3-64 to 3-85.
- [31] J. Mahaffey, D. Adam, A. Kalra, M. Anderson, and K. Sridharan, "Corrosion of Nickel-Base Alloys," in *Proceedings: EPRI International Conference on Corrosion in Power Plants*, EPRI-3002006972, Palo Alto, CA, 2015, pp. 3-19 to 3-46.